Chemical Engineering Science 264 (2022) 118134

Contents lists available at ScienceDirect

Chemical Engineering Science

journal homepage: www.elsevier.com/locate/ces

Mobility of trapped droplets within porous surfaces

Si Suo [a,c,d], Haibo Zhao [a], Shervin Bagheri [d], Peng Yu [a,*], Yixiang Gan [b,e,*]

[a] Department of Mechanics and Aerospace Engineering, Southern University of Science and Technology, China
[b] School of Civil Engineering, The University of Sydney, Australia
[c] State Key Laboratory for Strength and Vibration of Mechanical Structures, Xi'an, China
[d] Department of Mechanics, KTH Royal Institute of Technology, 100 44 Stockholm, Sweden
[e] The University of Sydney Nano Institute (Sydney Nano), The University of Sydney, NSW 2006, Australia

HIGHLIGHTS

- A 3D numerical model is built for studying the mobility of trapped droplets.
- Three mobility modes are identified covering a wide range of flow conditions.
- A pore-scale capillary number is proposed to characterize the droplet mobility.

GRAPHICAL ABSTRACT

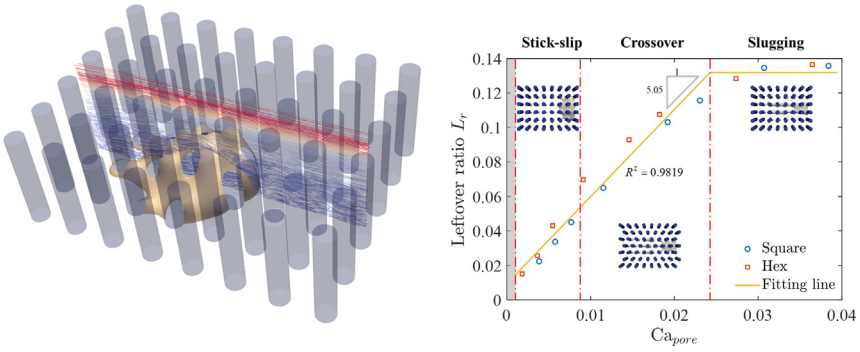

ARTICLE INFO

Article history:
Received 1 May 2022
Received in revised form 8 September 2022
Accepted 18 September 2022
Available online 24 September 2022

Keywords:
Droplet mobility
Porous surfaces
Capillary effects
Stain removal

ABSTRACT

Droplet mobility is essential in a wide range of engineering applications, e.g., fog collection and self-cleaning surfaces. For structured surfaces to achieve superhydrophobicity, the removal of stains adhered within the microscale surface features strongly determines the functional performance and durability. In this study, we numerically investigate the mobility of the droplet trapped within porous surfaces. Through simulations covering a wide range of flow conditions and porous geometries, three droplet mobility modes are identified, i.e., the stick–slip, crossover, and slugging modes. To quantitatively characterise the droplet dynamics, we propose a droplet-scale capillary number that considers the driving force and capillary resistance. By comparing against the simulation results, the proposed dimensionless number presents a strong correlation with the leftover volume. The dominating mechanisms revealed in this study provide a basis for further research on enhancing surface cleaning and optimising design of anti-fouling surfaces.

1. Introduction

Understanding droplet deformation, spreading, pinning, splitting, etc., is fundamental to engineering processes, e.g., water management in fuel cells (Mukherjee et al., 2009; Bazylak et al., 2008); enhanced oil recovery (Wang, 2021), and surface cleaning and coating (Thoreau et al., 2006; Christodoulou et al., 2018). The primary setting of shear flow passing a droplet adhering to a solid wall has been extensively investigated through experiments and numerical simulations. Before the onset of motion on a smooth wall, the resting droplet deforms under the shear flow until it reaches a critical stage with the increasing shear rate. Numerical

* Corresponding authors.
E-mail addresses: yup6@sustech.edu.cn (P. Yu), yixiang.gan@sydney.edu.au (Y. Gan).

https://doi.org/10.1016/j.ces.2022.118134
0009-2509/

studies indicated that the steady-state droplet shape is a consequence of the competition among viscous, capillary, and inertial effects (Dimitrakopoulos and Higdon, 1998; Dimitrakopoulos, 2007). The critical conditions can be characterized by capillary number (Ca) and Weber number (We), as a function of Reynolds number (Re) and contact angle hysteresis. Specifically, in the creeping-flow regime ($Re \ll 1$), only the shear stress needs to be balanced by the capillary force corresponding to a constant critical Ca and linearly increased We with Re (Dimitrakopoulos and Higdon, 1998; Dimitrakopoulos and Higdon, 1997); while with Re increasing to a moderate value (Re greater than 1), the inertial effect should be considered and thus the corresponding critical We nonlinearly increases and eventually approaches to a constant value (Ding and Spelt, 2008; Spelt, 2006). Similar conclusions were also reported from the theoretical analysis (Dussan, 1987) and experimental observations (Thoreau et al., 2006; Seevaratnam et al., 2010). Once a droplet is initiated to move, a variety of motion patterns are observed depending on the various combinations of fluid and surface properties. It was experimentally revealed that with increasing droplet viscosity and surface wettability, the droplet tends to be *slugging*, i.e., from moving as a whole to sliding with a trailing tail behind the droplet (Fan et al., 2011). As a consequence of larger droplet volume, it is possible to observe that the droplet may be lifted off the surface following the deformation and sliding (Seevaratnam et al., 2010; Madani and Amirfazli, 2014), i.e., droplet pinch-off and detachment. External factors, e.g., surfactants (Liu et al., 2020) or electricity fields (Raman et al., 2020), may also influence droplet behaviors.

As already mentioned, droplet processes are relevant in many engineering fields, like water management in fuel cells (Theodorakakos et al., 2006; Kumbur et al., 2006) which plays an essential role in their performance and long-term maintenance. During the fuel cell operation, the water produced from electrochemical reactions is transported and accumulated on the gas diffusion layers (GDLs) forming distinct droplets. The liquid removal mainly depends on the droplet movement driven by the air stream. This flow process has been studied widely (Niblett, 2020; Jeon and Kim, 2015; Xu et al., 2017), especially regarding the impact of surface roughness on the wetting and detachment of the droplets adhered to GDLs. Specifically, the roughness can alter the apparent surface wettability, i.e., the rougher the surface is, the more likely that the droplet touches GDLs in the Cassie mode (only the top is wetted) rather than the Wenzel mode (the porous zone is also wetted) and therefore promoting detachment (Bao and Gan, 2020); additionally, the roughness may affect the moving trail of a droplet resulting in a deviation from the channel center and touching the channel walls (Hou et al., 2020). On the other hand, the microstructure of GDLs can be artificially designed to assist the droplet motion (Chen et al., 2013).

Understanding how surface roughness and porosity impact droplet mobility not only contributes to optimizing the design of fuel cells but is also relevant for enhanced oil recovery at a much larger scale. Traditionally, oil recovery depends on the flooding displacement from fractured reservoirs (Akai et al., 2019; Nilsson et al., 2013; Yun et al., 2020). However, interfacial instabilities, such as viscous or capillary fingering, can result in undesired oil entrapping within pore space (Pak et al., 2015; Li et al., 2017). Further collecting the trapped oil phase is key to improving the recovery efficiency. Thus, gaining further knowledge of ganglia motion within flow paths containing complex surfaces is necessary.

In recent decades, a variety of artificial textured surfaces have been proposed for anti-icing (Hou, 2020), self-cleaning (Dalawai, 2020), superhydrophobicity (Dong et al., 2021; Yu et al., 2020), etc. Current research on droplet mobility mainly focuses on two aspects; droplet impact on solid surfaces and its post-impact effects including splashing, spreading, bouncing, sticking, gas trapping, etc. (Yada et al., 2021; Yarin, 2006); and spontaneous or programmable liquid movement along designed pathways (Sun et al., 2008; Lu et al., 2020), even anti-gravity climbing (Grounds et al., 2012; De Jong et al., 2019). To advance the field of artificial surfaces in engineering practice, we still need comprehensive knowledge regarding the droplet-surface wetting processes. Especially, when the functional surfaces are exposed to complex environments, such as varying temperature and humidity, liquid may be trapped within surficial microstructures, as shown in Fig. 1, which could impede the surface functionality. Therefore, understanding the dynamics of trapped liquid is especially important to liquid-repellant surfaces and the long-term maintenance of functional surfaces. Regarding droplet-porous matrix interactions, the focus of current research efforts is within the regimes of high mobility, e.g., bubbles flowing through saturated granular beds (Zinchenko and Davis, 2006; Zinchenko and Davis, 2017), high speed, e.g., droplet impacting on or through porous media (Wang et al., 2020; Liu et al., 2018; Tan, 2016), or quasi-static state, e.g., droplet settling on the porous surfaces (Suo et al., 2020; Markicevic et al., 2009; Suo and Gan, 2020). However, to the authors' knowledge, there are few studies directly related to the mobility of droplet trapped within porous surfaces.

To address this need, we investigate the process of a droplet trapped in the porous surface being displaced through 3D pore-scale simulations. We focus on droplets whose characteristic length is smaller than the surface feature size, and thus *within* the surface structure. In the Darcy-flow regime, the droplet behavior is determined by the competition between viscous and capillary effects. We demonstrate a transition of droplet motion mode, i.e., from capillary-dominated stick–slip mode to viscous-dominated slugging mode. A pore-scale capillary number is proposed by considering the tortuosity of obstacle arrangements to characterize

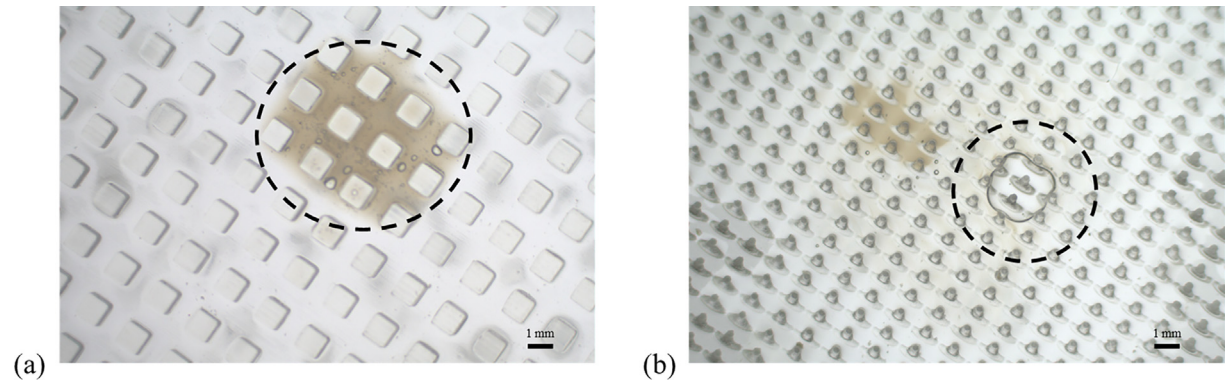

Fig. 1. Trapped liquid stain within the artificial surfaces, marked by black dash circles on patterned surface structures with: (a) square pillars, and (b) round pillars.

the mode transition. By a correlation analysis on the liquid leftover, we discover that the leftover volume is approximately proportional to the pore-scale capillary number and reaches a maximum value when slugging occurs. The current work sheds light on the droplet -porous media interaction in the Darcy-flow regime, and the discovered mechanism of droplet motion transition may pave the way to enhanced surface cleaning.

2. Numerical model

2.1. Numerical methods

In this study, we adopt the volume of fluid (VOF) to capture the droplet dynamics as it has been proved efficient and effective in pore-scale simulation (Das et al., 2018; Shams et al., 2018; Mirjalili et al., 2019). For incompressible two-phase flows, the governing equations, including the continuity equation, phase fraction equation, and momentum equation, are shown as.

$$\nabla \cdot \boldsymbol{u} = 0 \tag{1}$$

$$\frac{\partial \alpha}{\partial t} + \nabla \cdot (\boldsymbol{u}\alpha) = 0 \tag{2}$$

$$\rho \frac{\partial \boldsymbol{u}}{\partial t} + \rho(\boldsymbol{u} \cdot \nabla)\boldsymbol{u} = -\nabla p + \nabla \cdot \eta\left(\nabla \boldsymbol{u} + \nabla \boldsymbol{u}^T\right) + \mathbf{f}_\sigma \tag{3}$$

Here α is the phase fraction of two fluids, $\boldsymbol{u}$ represents the velocity field, ρ and η represent the weighted average of density and viscosity, respectively, i.e., $\rho = \alpha\rho_{f1} + (1-\alpha)\rho_{f2}$ and $\eta = \alpha\eta_{f1} + (1-\alpha)\eta_{f2}$, and p is the pressure. The surface tension $\mathbf{f}_\sigma$ is modelled as a continuum surface force (Brackbill et al., 1992);

$$\mathbf{f}_\sigma = \sigma\kappa\nabla\alpha \tag{4}$$

where σ is the surface tension and κ is the local interface curvature related to the normal direction of the interface $\boldsymbol{n}_\alpha$, i.e.,

$$\boldsymbol{n}_\alpha = -\frac{\nabla\alpha}{|\nabla\alpha|} \tag{5}$$

$$\kappa = -\nabla \cdot \boldsymbol{n}_\alpha \tag{6}$$

The partial wetting conditions on solid surfaces can be applied by adjusting the interface normal,

$$\boldsymbol{n}_\alpha = \boldsymbol{n}_s \cos(\theta_w) + \boldsymbol{\tau}_s \sin(\theta_w) \tag{7}$$

where $\boldsymbol{n}_s$ and $\boldsymbol{\tau}_s$ are the normal and tangential vectors of solid surfaces, respectively, and θ_w is the equilibrium contact angle. Regarding the implementation of partially wetting conditions and inlet–outlet boundaries, one can refer to (Linder, 2015). The numerical solution of Eqs. (1 ∼ 3) plus boundary conditions is obtained by using OpenFoam, an open source CFD toolbox, and more relative parameters and settings regarding the numerical modelling are as follows.

As shown in Fig. 2, the simulations are conducted in a 3D domain with patterned obstacles to represent the porous surface, which are arranged in two forms, i.e., square and hexagon arrays. By adjusting obstacle radius, both arrangements possess the same porosity and throat size. The geometric parameters of two arrangements are summarized in Table 1. A pressure difference ΔP is applied between the left (inlet) and right (outlet) boundaries, and the top face of the computation domain is set to be an open boundary. Regarding velocity boundaries, zero-flux conditions are applied. Surfaces of the bottom and obstacles are wettable no-slip walls with a given constant contact angle θ_w of 60° without hysteresis considered in this work. The droplet is initially placed close to the inlet with radius r_d of 3 mm, which indicates the radius of the initial sessile droplet sitting on the bottom surface with the specified contact angle, see Table 1 for how r_d compares with obstacle size and throat size. Other initial conditions include zero velocity and pressure everywhere.

The pioneering works regarding droplet mobility (Golpaygan and Ashgriz, 2005; Golpaygan and Ashgriz, 2008) suggested that the behavior of droplets is determined by the combined effects involving capillary, viscous and inertial forces. Thus, to comprehensively investigate the mobility of a trapped droplet within porous surfaces, besides the varied porous geometries as above, the driving pressure and surface tension cover a wide range, i.e., $\Delta P = 100\ 2000$ Pa and $\sigma = 36\ 144$ mN/m. As for fluid properties, the ambient and droplet fluids are assumed to have the same viscosity $\eta_A = \eta_D = 1$ mPa·s, and density $\rho_A = \rho_D = 1 \times 10^3$ kg/m^3.

2.2. Mesh sensitivity

To balance the numerical accuracy and computational cost, we design the meshing scheme for the computation domain as shown in Fig. 3(a). Specifically, the whole computational domain is

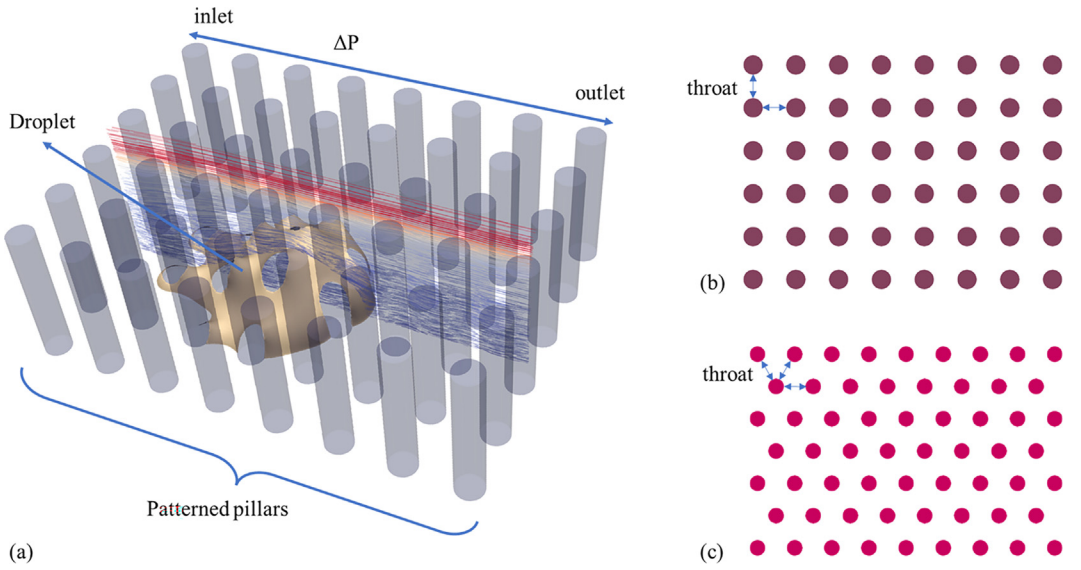

Fig. 2. (a) The schematic of pore-scale numerical model, i.e., a trapped droplet is driven by pressure difference ΔP from inlet to outlet and moves through a porous surface, whose solid space is composed of patterned round pillars arranged in two forms, i.e., (b) square array and (c) hexagon array.

Table 1
Geometric parameters of the square and hex arrangement (Ref: $r_d = 3$ mm).

	porosity ϕ[/]	throat size r_t [mm]	obstacle radius r_r [mm]	tortuosity τ [/]	permeability K[mm^2]
Square	0.84	1.4	0.56	1.0179	39.9
Hex	0.84	1.4	0.50	1.1715	16.5

*Refer to Appendix for obtaining the permeability and tortuosity.

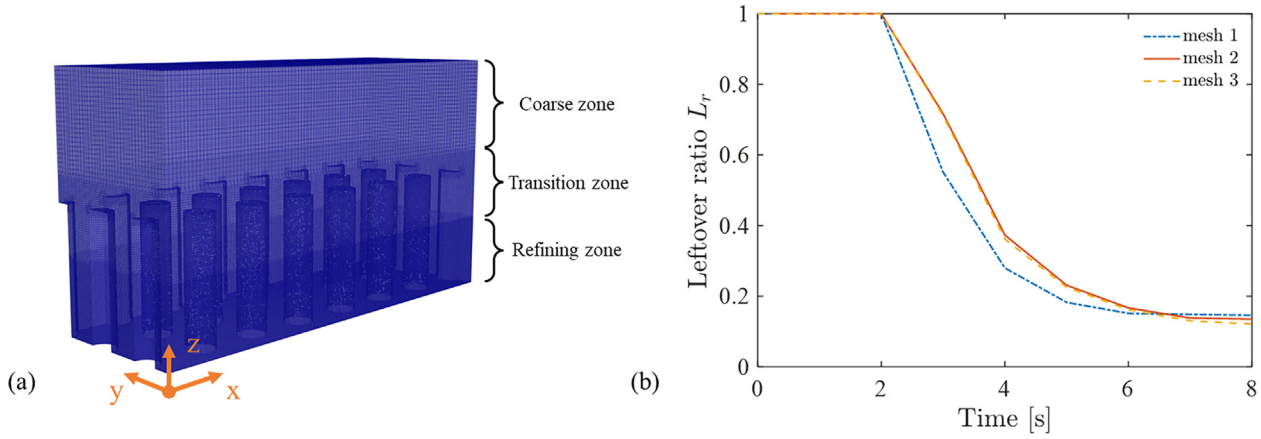

Fig. 3. (a) The meshing scheme of the numerical model, including a coarse zone, a refined zone and a transition zone. (b) The comparison on the leftover ratio among three meshing schemes under the flow condition of $\Delta P = 1000$ Pa and $\sigma = 72$ mN/m.

divided into three zones, i.e., the coarse zone on the top covering the free-surface flow domain, where the mesh size Δx_c is regarded as a reference and fixed as 0.17 mm leading to at least 10 grids across a throat, see below and Table 1. The refined zone on the bottom of the porous domain covers the droplet moving region, where the mesh size Δx_r is refined compared with Δx_c. These two zones are bridged by a transition zone. An index, leftover ratio L_r, defined as a ratio of the total leftover liquid volume inside the computation domain to the initial droplet volume, is used to measure the convergence of the mesh-dependence study. Three mesh schemes, i.e., mesh 1 ($\Delta x_r = \Delta x_c/2$), mesh 2 ($\Delta x_r = \Delta x_c/4$), mesh 3 ($\Delta x_r = \Delta x_c/8$) are tested and compared, as shown in Fig. 3(b). The results of mesh 2 and 3 overlap, and therefore mesh 2 is adopted in the following simulations. Additionally, an adjustable time step is adopted for simulation and the time step is determined according to the Courant number ($\frac{u_{\max}\Delta t}{\Delta x_r}$) (Courant and Friedrichs, 1999) limit set as 0.5 here. The average time step for mesh 2 is around 1×10^{-5} s, which can guarantee a stable and precise solution.

3. Results and discussion

For a moving droplet adhered to a solid surface, three modes of motion, namely sliding, crawling and detachment, can be observed depending on surface properties and flow conditions (Seevaratnam et al., 2010; Fan et al., 2011). However, the mobility of a moving droplet trapped in a porous surface is more complex since the flow dynamics and interface morphology are strongly modified by the solid structures. The process involves droplet splitting, attaching, and spreading, as a result of the interaction between viscous and capillary effects. Within a limited domain (17.5 mm × 12.5 mm), the process can be generally divided into pre- and post-drain-out stages. The moment when the rear of a droplet leaves the outlet and part of liquid is left behind and attached to the obstacles is defined as the "drain-out" state. In this study, we focus on the droplet motion during the pre-drain-out stage.

To characterize the droplet motion at the pre-drain-out stage, the capillary number, defined as the ratio of viscous force to capillary force, is adopted (Ding et al., 2010). The capillary force can be represented by the surface tension force σr_d, while the viscous force can be estimated from the characteristic flow velocity, i.e., $\eta_A \bar{U} r_d$. For modelling fluid flow through porous media, the Brinkman model is a common choice (Koplik, 1983; Auriault, 2009), and it can be regarded as an empirical extension of the Darcy's law since the Brinkmann model involves a velocity gradient term to consider the large shear if it occurs. Thus, the Brinkman model is suitable for the situation with very large permeability or fast flow (the inertial effect is still neglected), otherwise the Brinkman model is recovered to Darcy's law (Koplik, 1983; Auriault, 2009). In this work, the Reynolds number $\mathrm{Re} = \frac{\rho_A \bar{U} r_r}{\eta_A} \leq 0.65$, where r_r is the obstacle radius, and therefore the flow is kept very slow and the Darcy's law can properly estimate the flow rate $\bar{U}$. According to the Darcy's law, the field-average flow velocity U_{Darcy} is.

$$U_{\mathrm{Darcy}} = \frac{K}{\eta_A}\frac{\Delta P}{L} \tag{8}$$

where L is the length of the domain from the inlet to the outlet. However, compared with the field-scale length, the droplet size is much smaller and comparable to the pore or throat size. Therefore, the droplet motion is controlled by the local flow field and a pore-scale quantity can better work as a characteristic flow rate. Here, the tortuosity is introduced to further modify the U_{Darcy} as a pore-scale average flow rate U_{pore} (Ghanbarian et al., 2013);

$$U_{\mathrm{pore}} = \frac{U_{\mathrm{Darcy}}}{\phi}\tau \tag{9}$$

We adopt U_{pore} as the characteristic velocity $\bar{U}$, and finally the pore-scale capillary number is obtained as.

$$\mathrm{Ca}_{\mathrm{pore}} = \frac{\eta_A U_{\mathrm{pore}}}{\sigma} = \frac{\tau K}{\phi L}\frac{\Delta P}{\sigma} \tag{10}$$

which is adopted to describe the interaction between capillary and viscous effects during droplet motion for the following analysis.

3.1. Simulation results

By using the numerical model presented in Section 2, simulations of the trapped droplet moving through a porous surface are performed under various flow and geometric conditions. The results suggest that the moving processes can be divided into three motion modes, i.e., the stick–slip, crossover, and slugging mode, as shown in Fig. 4. For the *stick–slip* mode, the droplet behavior is controlled by the capillary effects, i.e., Ca_{pore} is smaller than 0.01. The droplet almost retains its initial shape, and the interface is displaced pore-by-pore. Noticeably, as marked by yellow circles in Fig. 4(a), when the rear interface crosses the obstacles, a suction force induced by the curved interface is exerted on the meniscus. The direction, which is indicated by a red arrow marked in Fig. 4 (a), leads to droplet splitting and partial liquid attaching to the obstacles as a leftover component. Unlike the stick–slip mode, the *slugging* mode is dominated by the viscous effects, i.e., Ca_{pore} is comparably larger than 0.02. Specifically, the droplet spreads as a thin film and its interface moves much faster along the main channels than in the down-wind pore space due to the increased viscous resistance. As a consequence, liquid tails are left behind the droplet and wrapped around obstacles, as marked by red circles in Fig. 4(c), which may further be snapped off into smaller sub-droplets attached obstacles. Bridging the stick–slip and slugging modes, the *crossover* mode is observed around the balance point of viscous and capillary effects, resulting in the mixed features of the other two modes. The kinematics of these motion modes are further illustrated in the supplementary animations.

In sum, the mobility of droplets is determined by the competition between the capillary and viscous effects, which also controls the droplet rupture mechanisms. For the stick–slip mode, the droplet rupture is induced by the capillary force, and it is similar with the liquid bridge breakup (Suo and Gan, 2020; Tourtit et al., 2019). However, for the slugging mode, the interface dynamics lose stability, and thus the droplet tends to be a thin film along the z-axis direction and ruptured within the x-y plane due to the strong shear stress. So, to this extent, this phenomenon is closer to the Saffman-Taylor instability and similar processes can be referred to the "dewetting in capillary tubes" (Gao et al., 2019; Zhao et al., 2018).

Once the droplet leaves the region of interest from the outlet, part of it remains within the porous surfaces in the form of smaller drops or long slugs sticking to the obstacles. The distribution of the remaining liquid volume of drops or slugs can further characterize the motion modes. Fig. 5 shows the cumulative distribution function (CDF) F of remaining drop volumes, defined as a proportion of drops smaller than a given volume $\bar{V}_d$ normalized by the initial droplet volume. For the stick–slip mode, the droplet marches slowly and stably like a quasi-static process so that the droplet is split evenly and the liquid volume distributes within a narrow range, i.e., the remaining drops share the similar size. By contrast, the liquid volumes of the slugging mode cover a much wider range because the droplet spreads fast and long slugs occur. In crossover mode, the CDF mostly lies in the middle since the small drops and short slugs co-exist.

We can use the index L_r to describe the displacing process. The change of L_r is directly related to the switch of droplet motion modes, i.e., it is expected to be small for the stick–slip mode and large for the slugging mode. Simulation results, as demonstrated in Fig. 4, suggest that conditions that are related to the viscous and capillary effects can trigger the switch of droplet motion modes and finally contribute to the leftover ratio. Specifically, with the driving pressure increasing, as shown in Fig. 6(a), the viscous effect is enhanced, i.e., Ca_{pore} increases from 0.0038 to 0.0384, and thus droplet motion experiences a transition from the stick–slip to slugging mode as indicated in Fig. 4. Correspondingly, the drain-out leftover ratio increases more than 10%. Also, the average droplet moving speed, which can be estimated by the drain-out time, increases with driving pressure. The surface tension directly contributes to the capillary effects, and with its increment as shown in Fig. 6(b) from I ($Ca_{pore} = 0.0230$), II ($Ca_{pore} = 0.0115$) to III ($Ca_{pore} = 0.0058$), the droplet motion tends to follow the stick–slip mode. In general, both the viscous and capillary effects depend on the geometry. The capillary force is mainly determined by the porosity and throat size (Suo and Gan, 2020), which are the same for the two configuration (see Table 1). The viscous effects on the other hand are different for the two different arrangements, due to the significant difference in the permeability of both configurations (see Table 1). The effective flow rate of the square arrangement is larger than that of the hex arrangement under the same driving pressure and correspondingly larger for Ca_{pore} in the square arrangement so that the droplet motion within the square arrangement is closer to the slugging mode, as shown in Fig. 6(c).

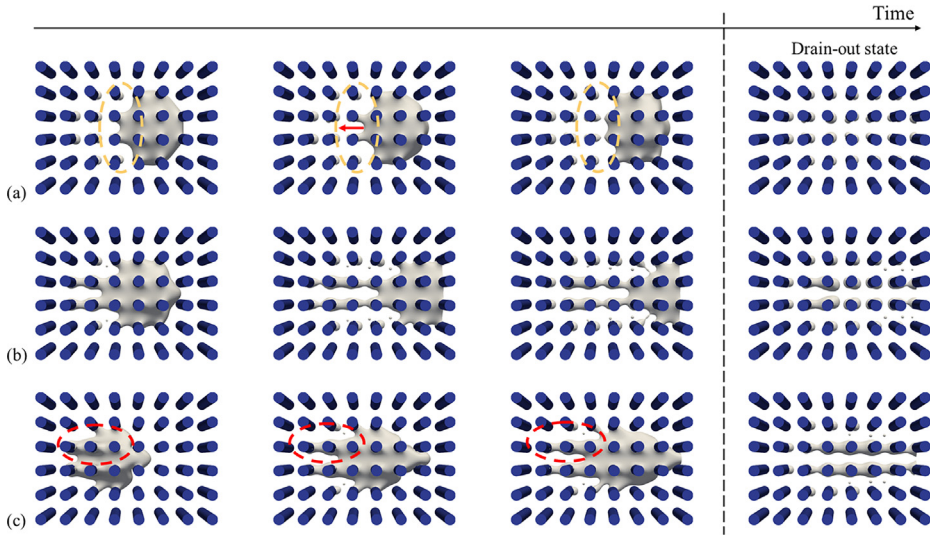

Fig. 4. The evolution of three droplet motion modes in square arrangement: (a) stick–slip mode ($\Delta P = 200$ Pa, $\sigma = 72$ mN/m, $Ca_{pore} = 0.0077$), (b) crossover mode ($\Delta P = 500$ Pa, $\sigma = 72$ mN/m, $Ca_{pore} = 0.0192$), and (c) slugging mode ($\Delta P = 1000$ Pa, $\sigma = 72$ mN/m, $Ca_{pore} = 0.0384$). The last column indicates the liquid distribution of each mode at the drain-out state.

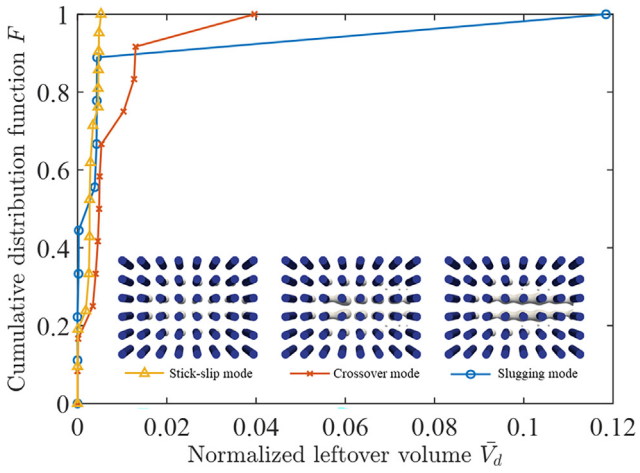

Fig. 5. Cumulative distribution function of dispersed liquid leftover volumes at the drain-out state, which are normalized by the initial droplet volume, for three motion modes.

In summary, the competition between capillary and viscous effects controls the behavior of a trapped droplet moving through a porous surface, and correspondingly determines the liquid leftover which could be a useful quantity in patterned surface optimization and flow process design, especially for surface cleaning engineering. So, we conducted a correlation analysis as follows to build a quantitative description of drain-out state leftover ratio.

3.2. Correlation analysis

The drain-out state leftover ratio L_r as a function of $\mathrm{Ca}_{\mathrm{pore}}$ is shown in Fig. 7. At the first domain, covering the stick–slip and crossover mode, L_r monotonically increases with $\mathrm{Ca}_{\mathrm{pore}}$ and approximately follows linear relationship, i.e.,

$$L_r = \lambda \mathrm{Ca}_{\mathrm{pore}} + L_r^0 \tag{11}$$

where λ is the scale coefficient and L_r^0 is the vertical intercept. The simulation data for both configurations can collapse on this fitting line as shown in Fig. 7, and the function of $\mathrm{Ca}_{\mathrm{pore}}$ to L_r matches the proposed model in Eq. (11) with R^2 = 0.9819. Then, when $\mathrm{Ca}_{\mathrm{pore}}$ is beyond 0.0230, L_r enters a plateau which indicates that the slugging mode occurs and the maximum volume of the droplet are trapped as long slugs. If the driving pressure further increases, inertial effects may be involved, and the droplet pinch-off is expected, which is beyond the scope of this study. Noticeably, if the viscous force is too small to overcome the capillary barrier, corresponding to a threshold value of $\mathrm{Ca}_{\mathrm{pore}} \leq 0.0015$, marked by the grey area in Fig. 7, the droplet is stationary due to pinning.

It should be noted that the proposed pore-scale capillary number, $\mathrm{Ca}_{\mathrm{pore}}$, unifies the results from different array types considered

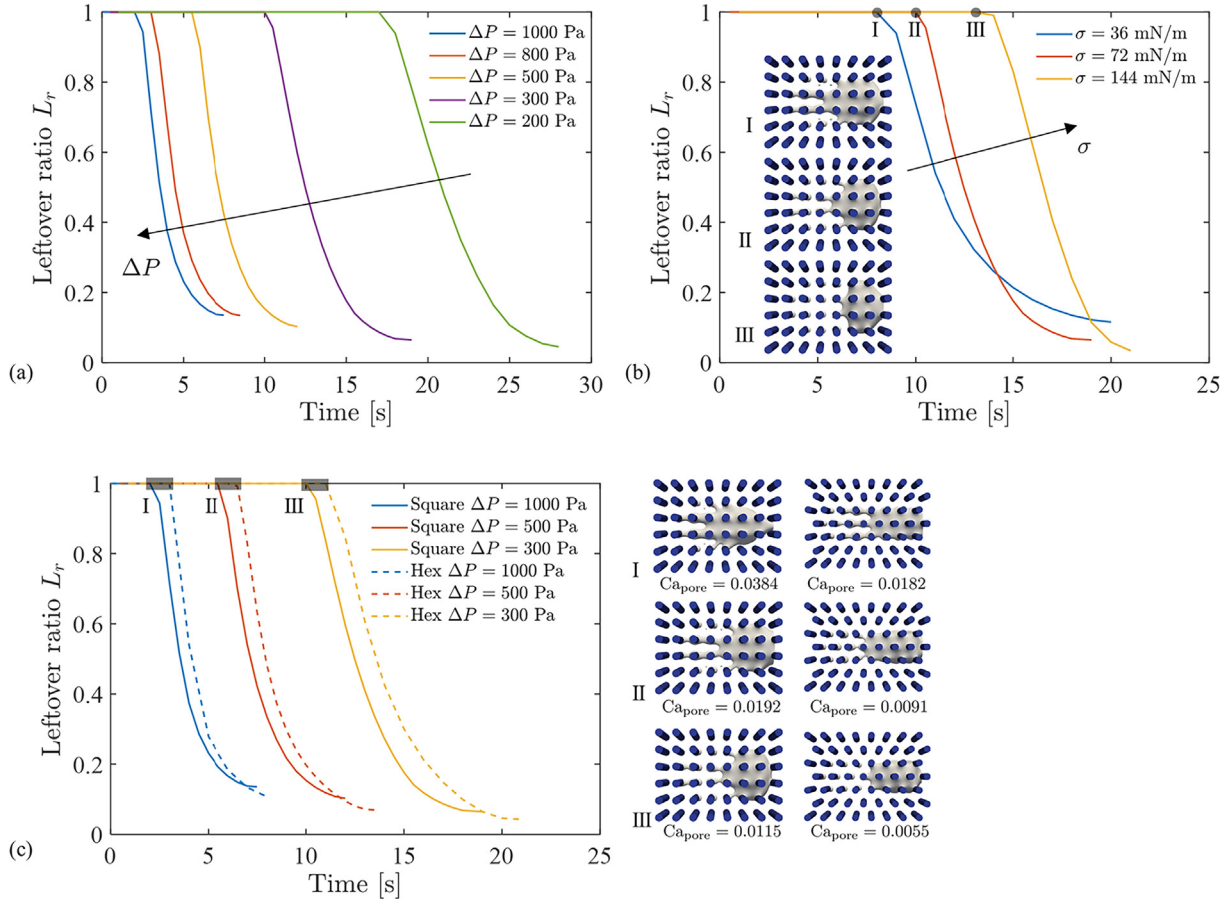

Fig. 6. The evolution of leftover ratio L_r from the onset to the drain-out state for different cases: (a) square arrangement with $\sigma = 72$ mN/m and $\Delta P = 200, 300, 500, 800$ and 1000 Pa; (b) square arrangement, $\Delta P = 300$ Pa, $\sigma = 36, 72$ and 144 mN/m; (c) comparison between square and hex arrangement with $\sigma = 72$ mN/m and $\Delta P = 300, 500$ and 1000 Pa.

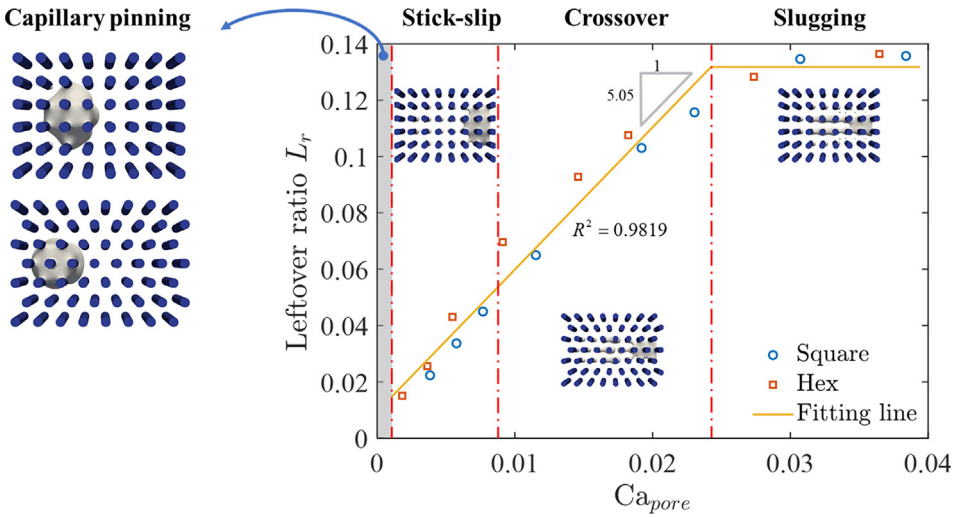

Fig. 7. Drain-out state leftover ratio L_r vs. pore-scale capillary number Ca_{pore}. The mode boundaries are marked by the red dot-dash line, as $Ca_{pore} \approx 0.0015$, 0.0090 and 0.0230.

in this study across a wide range of physical parameter space. The index can be used to guide and optimize the surface cleaning processes in practice for given fluid properties and surface structures.

4. Conclusion

In this work, we focus on the dynamics of a trapped droplet moving through porous surfaces, and the combined impacts of viscous and capillary forces on droplet mobility are numerically investigated by pore-scale simulations covering various flow conditions and geometric configurations. Specifically, three droplet motion modes are identified. With the continuous enhancement in the viscous effects relative to the capillary effects, the moving pattern transits from the stick–slip, crossover to slugging mode, and the remaining liquid forms separate drops, short slugs to long slugs, correspondingly. The droplet mobility and transition of its motion modes are a consequence of the competition between viscous and capillary effects, and therefore can be naturally characterized by the proposed capillary number Ca_{pore}, which captures the pore scale flow conditions. Furthermore, we find a strong correlation between Ca_{pore} and the drain-out state leftover ratio L_r, which presents two domains, i.e., L_r linearly increases with Ca_{pore} at the first domain covering the stick–slip and crossover modes; and L_r reaches the maximum value and enters a plateau once the long slugs occurs at $Ca_{pore} \approx 0.0230$. The conclusion of this study can provide guidance on optimizing the design of patterned surfaces, especially for the anti-fouling features as well as surface cleaning improvement. Furthermore, knowledge of the inertial-involved processes is worth exploring as an extension of this work since it may benefit the engineering involving liquid atomization and droplet dispersion, etc.

CRediT authorship contribution statement

Si Suo: Conceptualization, Methodology, Software, Validation, Writing – original draft, Visualization. **Haibo Zhao:** Conceptualization, Methodology. **Shervin Bagheri:** Conceptualization, Writing – review & editing. **Peng Yu:** Conceptualization, Supervision, Writing – review & editing. **Yixiang Gan:** Conceptualization, Supervision, Writing – review & editing.

Declaration of Competing Interest

The authors declare that they have no known competing financial interests or personal relationships that could have appeared to influence the work reported in this paper.

Acknowledgement

This work was supported by the National Natural Science Foundation of China (Grant No. 12172163 and 91852205) and the Open Project Funding (Grant No. SV2021-KF-27) from State Key Laboratory for Strength and Vibration of Mechanical Structures.

Appendix

In this appendix, details on obtaining the permeability and tortuosity of two porous surfaces are demonstrated. We solve the single-phase flow field based on the same geometries, meshes and parameters as the two-phase flow, i.e., Eq. (1) and (3) without $\mathbf{f}_\sigma$. For the permeability, it comes from Darcy's law, and thus can be obtained from fitting the average flow rate $\bar{U}$ directly measured from the outlet boundary and the pressure gradient $\frac{\Delta P}{L}$, as shown in Fig. A1. Furthermore, the streamlines can be calculated based

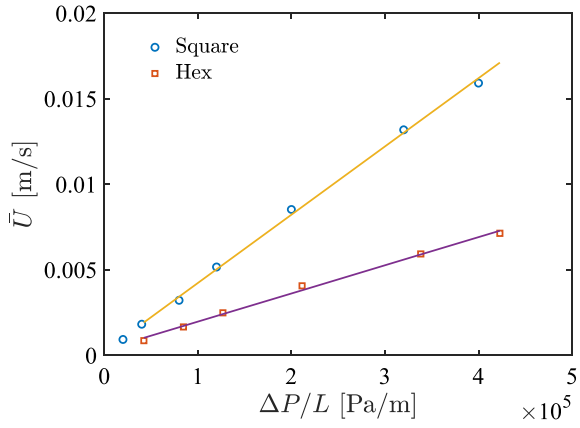

Fig. A1. The average rate $\bar{U}$ vs. the pressure gradient $\frac{\Delta P}{L}$.

on the flow field and the tortuosity can be estimated as a ratio between the average streamline length and the domain length L.

References

Mukherjee, P.P., Wang, C.-Y., Kang, Q., 2009. Mesoscopic modeling of two-phase behavior and flooding phenomena in polymer electrolyte fuel cells. Electrochim. Acta 54 (27), 6861–6875.

Bazylak, A., Sinton, D., Djilali, N., 2008. Dynamic water transport and droplet emergence in PEMFC gas diffusion layers. J. Power Sources 176 (1), 240–246.

Wang, F., Liu, T., Lei, W.B., Zhao, Y., Li, B., Yang, G., Liu, Y., Wang, M., 2021. Dynamic analysis of deformation and start-up process of residual-oil droplet on wall under shear flow. J. Petrol. Sci. Eng. 199, 108335.

Thoreau, V., Malki, B., Berthome, G., Boulange-Petermann, L., Joud, J.C., 2006. Physico-chemical and dynamic study of oil-drop removal from bare and coated stainless-steel surfaces. J. Adhes. Sci. Technol. 20 (16), 1819–1831.

Christodoulou, C., Sorensen, E., García-Muñoz, S., Mazzei, L., 2018. Mathematical modelling of water absorption and evaporation in a pharmaceutical tablet during film coating. Chem. Eng. Sci. 175, 40–55.

Dimitrakopoulos, P., Higdon, J.J.L., 1998. On the displacement of three-dimensional fluid droplets from solid surfaces in low-Reynolds-number shear flows. J. Fluid Mech. 377, 189–222.

Dimitrakopoulos, P., 2007. Deformation of a droplet adhering to a solid surface in shear flow: onset of interfacial sliding. J. Fluid Mech. 580, 451.

Dimitrakopoulos, P., Higdon, J.J.L., 1997. Displacement of fluid droplets from solid surfaces in low-Reynolds-number shear flows. J. Fluid Mech. 336, 351–378.

Ding, H., Spelt, P.D.M., 2008. Onset of motion of a three-dimensional droplet on a wall in shear flow at moderate Reynolds numbers. J. Fluid Mech. 599, 341–362.

Spelt, P.D., 2006. Shear flow past two-dimensional droplets pinned or moving on an adhering channel wall at moderate Reynolds numbers: a numerical study. J. Fluid Mech. 561 (439), 8.

Dussan, V.E., 1987. On the ability of drops to stick to surfaces of solids. Part 3. the influences of the motion of the surrounding fluid on dislodging drops. J. Fluid Mech. 174 (-1), 381–397.

Seevaratnam, G.K., Ding, H., Michel, O., Heng, J.Y.Y., Matar, O.K., 2010. Laminar flow deformation of a droplet adhering to a wall in a channel. Chem. Eng. Sci. 65 (16), 4523–4534.

Fan, J., Wilson, M.C.T., Kapur, N., 2011. Displacement of liquid droplets on a surface by a shearing air flow. J. Colloid Interface Sci. 356 (1), 286–292.

Madani, S., Amirfazli, A., 2014. Oil drop shedding from solid substrates by a shearing liquid. Colloids Surf., A 441, 796–806.

Liu, H., Zhang, J., Ba, Y., Wang, N., Wu, L., 2020. Modelling a surfactant-covered droplet on a solid surface in three-dimensional shear flow. J. Fluid Mech. 897.

Raman, K.A., Birgersson, E., Sui, Y., Fisher, A., 2020. Electrically induced droplet ejection dynamics under shear flow. Phys. Fluids 32 (3).

Theodorakakos, A., Ous, T., Gavaises, M., Nouri, J.M., Nikolopoulos, N., Yanagihara, H., 2006. Dynamics of water droplets detached from porous surfaces of relevance to PEM fuel cells. J. Colloid Interface Sci. 300 (2), 673–687.

Kumbur, E.C., Sharp, K.V., Mench, M.M., 2006. Liquid droplet behavior and instability in a polymer electrolyte fuel cell flow channel. J. Power Sources 161 (1), 333–345.

Niblett, D., Mularczyk, A., Niasar, V., Eller, J., Holmes, S., 2020. Two-phase flow dynamics in a gas diffusion layer - gas channel - microporous layer system. J. Power Sources 471, 228427.

Jeon, D.H., Kim, H., 2015. Effect of compression on water transport in gas diffusion layer of polymer electrolyte membrane fuel cell using lattice Boltzmann method. J. Power Sources 294, 393–405.

Xu, A., Shyy, W., Zhao, T., 2017. Lattice Boltzmann modeling of transport phenomena in fuel cells and flow batteries. Acta Mech. Sin. 33 (3), 555–574.

Bao, Y., Gan, Y., 2020. Roughness effects of gas diffusion layers on droplet dynamics in PEMFC flow channels. Int. J. Hydrogen Energy 45 (35), 17869–17881.

Hou, Y., Deng, H., Zamel, N., Du, Q., Jiao, K., 2020. 3D lattice Boltzmann modeling of droplet motion in PEM fuel cell channel with realistic GDL microstructure and fluid properties. Int. J. Hydrogen Energy 45 (22), 12476–12488.

Chen, L., He, Y.-L., Tao, W.-Q., 2013. Effects of surface microstructures of gas diffusion layer on water droplet dynamic behaviors in a micro gas channel of proton exchange membrane fuel cells. Int. J. Heat Mass Transf. 60, 252–262.

Akai, T., Alhammadi, A.M., Blunt, M.J., Bijeljic, B., 2019. Modeling Oil Recovery in Mixed-Wet Rocks. Pore-Scale Comparison Between Experiment and Simulation. 127 (2), 393–414.

Nilsson, M.A., Kulkarni, R., Gerberich, L., Hammond, R., Singh, R., Baumhoff, E., Rothstein, J.P., 2013. Effect of fluid rheology on enhanced oil recovery in a microfluidic sandstone device. J. Nonnewton. Fluid Mech. 202, 112–119.

Yun, W., Chang, S., Cogswell, D.A., Eichmann, S.L., Gizzatov, A., Thomas, G., Al-Hazza, N., Abdel-Fattah, A., Wang, W., 2020. Toward reservoir-on-a-chip: rapid performance evaluation of enhanced oil recovery surfactants for carbonate reservoirs using a calcite-coated micromodel. Sci. Rep. 10 (1).

Pak, T., Butler, I.B., Geiger, S., van Dijke, M.I.J., Sorbie, K.S., 2015. Droplet fragmentation: 3D imaging of a previously unidentified pore-scale process during multiphase flow in porous media. Proc. Natl. Acad. Sci. 112 (7), 1947–1952.

Li, J., Jiang, H., Wang, C., Zhao, Y., Gao, Y., Pei, Y., Wang, C., Dong, H.u., 2017. Pore-scale investigation of microscopic remaining oil variation characteristics in water-wet sandstone using CT scanning. J. Nat. Gas Sci. Eng. 48, 36–45.

Hou, W., Shen, Y., Tao, J., Xu, Y., Jiang, J., Chen, H., Jia, Z., 2020. Anti-icing performance of the superhydrophobic surface with micro-cubic array structures fabricated by plasma etching. Colloids Surf., A 586, 124180.

Dalawai, S.P., Saad Aly, M.A., Latthe, S.S., Xing, R., Sultar, R.S., Nagappan, S., Ha, C., Kumar Sadasivuni, K., Liu, S., 2020. Recent Advances in durability of superhydrophobic self-cleaning technology: a critical review. Prog. Org. Coat. 138, 105381.

Dong, Z., Vuckovac, M., Cui, W., Zhou, Q., Ras, R.H.A., Levkin, P.A., 2021. 3D Printing of Superhydrophobic Objects with Bulk Nanostructure. Adv. Mater. 33 (45), 2106068.

Yu, C., Sasic, S., Liu, K., Salameh, S., Ras, R.H.A., van Ommen, J.R., 2020. Nature-Inspired self–cleaning surfaces: mechanisms, modelling, and manufacturing. Chem. Eng. Res. Des. 155, 48–65.

Yada, S., Allais, B., van der Wijngaart, W., Lundell, F., Amberg, G., Bagheri, S., 2021. Droplet impact on surfaces with asymmetric microscopic features. Langmuir 37 (36), 10849–10858.

Yarin, A.L., 2006. DROP Impact dynamics: splashing, spreading, receding, bouncing. Annu. Rev. Fluid Mech. 38 (1), 159–192.

Sun, C., Zhao, X.-W., Han, Y.-H., Gu, Z.-Z., 2008. Control of water droplet motion by alteration of roughness gradient on silicon wafer by laser surface treatment. Thin Solid Films 516 (12), 4059–4063.

Lu, Y., Shen, Y., Tao, J., Wu, Z., Chen, H., Jia, Z., Xu, Y., Xie, X., 2020. Droplet directional movement on the homogeneously structured superhydrophobic surface with the gradient non-wettability. Langmuir 36 (4), 880–888.

Grounds, A., Still, R., Takashina, K., 2012. Enhanced droplet control by transition Boiling. Sci. Rep. 2 (1).

De Jong, E., Wang, Y., Den Toonder, J.M.J., Onck, P.R., 2019. *Climbing droplets driven by mechanowetting on transverse waves.* Science. Advances 5 (6).

Zinchenko, A.Z., Davis, R.H., 2006. A boundary-integral study of a drop squeezing through interparticle constrictions. J. Fluid Mech. 564, 227.

Zinchenko, A.Z., Davis, R.H., 2017. Motion of deformable drops through porous media. Annu. Rev. Fluid Mech. 49 (1), 71–90.

Wang, G., Fei, L., Luo, K.H., 2020. Lattice Boltzmann simulation of water droplet impacting a hydrophobic plate with a cylindrical pore. Phys. Rev. Fluids 5, (8) 083602.

Liu, D., Tan, H.-W., Tran, T., 2018. Droplet impact on heated powder bed. Soft Matter 14 (48), 9967–9972.

Tan, H., 2016. Three-dimensional simulation of micrometer-sized droplet impact and penetration into the powder bed. Chem. Eng. Sci. 153, 93–107.

Suo, S., Liu, M., Gan, Y., 2020. An LBM-PNM framework for immiscible flow: With applications to droplet spreading on porous surfaces. Chem. Eng. Sci. 218, 115577.

Markicevic, B., Li, H., Sikorski, Y., Zand, A.R., Sanders, M., Navaz, H.K., 2009. Infiltration time and imprint shape of a sessile droplet imbibing porous medium. J. Colloid Interface Sci. 336 (2), 698–706.

Suo, S., Gan, Y., 2020. Rupture of Liquid Bridges on Porous Tips: Competing Mechanisms of Spontaneous Imbibition and Stretching. Langmuir 36 (45), 13642–13648.

Das, S., Patel, H.V., Milacic, E., Deen, N.G., Kuipers, J.A.M, 2018. Droplet spreading and capillary imbibition in a porous medium: a coupled IB-VOF method based numerical study. Phys. Fluids 30 (1).

Shams, M., Raeini, A.Q., Blunt, M.J., Bijeljic, B., 2018. A numerical model of two-phase flow at the micro-scale using the volume-of-fluid method. J. Comput. Phys. 357, 159–182.

Mirjalili, S., Ivey, C.B., Mani, A., 2019. Comparison between the diffuse interface and volume of fluid methods for simulating two-phase flows. Int. J. Multiph. Flow 116, 221–238.

Brackbill, J.U., Kothe, D.B., Zemach, C., 1992. A continuum method for modeling surface tension. J. Comput. Phys. 100 (2), 335–354.

Linder, N., 2015. *Numerical simulation of complex wetting*, in *maschinenbau*. Technische Universität, Darmstadt.

Golpaygan, A., Ashgriz, N., 2005. Effects of oxidant fluid properties on the mobility of water droplets in the channels of PEM fuel cell. Int. J. Energy Res. 29 (12), 1027–1040.

Golpaygan, A., Ashgriz, N., 2008. Multiphase flow model to study channel flow dynamics of PEM fuel cells: deformation and detachment of water droplets. Int. J. Comput. Fluid Dynamics 22 (1–2), 85–95.

R, Courant, K.O, Friedrichs, *Supersonic flow and shock waves*. Vol. 21. 1999: Springer Science & Business Media.

Ding, H., Gilani, M.N.H., Spelt, P.D.M., 2010. Sliding, pinch-off and detachment of a droplet on a wall in shear flow. J. Fluid Mech. 644, 217–244.

Koplik, J., 1983. Viscosity renormalization in the Brinkman equation. Phys. Fluids 26 (10), 2864.

Auriault, J.-L., 2009. On the domain of validity of brinkman's equation. Transp. Porous Media 79 (2), 215–223.

Ghanbarian, B., Hunt, A.G., Ewing, R.P., Sahimi, M., 2013. Tortuosity in porous media: a critical review. Soil Sci. Soc. Am. J. 77 (5), 1461–1477.

Tourtit, Y., Gilet, T., Lambert, P., 2019. Rupture of a Liquid Bridge between a Cone and a Plane. Langmuir 35 (37), 11979–11985.

Gao, P., Liu, A.o., Feng, J.J., Ding, H., Lu, X.-Y., 2019. Forced dewetting in a capillary tube. J. Fluid Mech. 859, 308–320.

Zhao, B., Alizadeh Pahlavan, A., Cueto-Felgueroso, L., Juanes, R., 2018. Forced wetting transition and bubble pinch-off in a capillary tube. Phys. Rev. Lett. 120, (8) 084501.